JOURNAL OF GEOPHYSICAL RESEARCH, VOL. 115, A01213, doi:10.1029/2009JA014443, 2010

The effect of smoothed solar wind inputs on global modeling results

Raluca Ilie,[1] Michael W. Liemohn,[1] and Aaron Ridley[1]

Received 9 May 2009; revised 18 August 2009; accepted 2 October 2009; published 27 January 2010.

[1] This study investigates the role of fluctuations in the solar wind parameters in triggering a magnetic storm and assesses the storm simulation ability of the Space Weather Modeling Framework (SWMF) through a model–data comparison. The event of 22 September 1999 is examined through global magnetosphere simulations, using as input Advanced Composition Explorer (ACE) observations (4 min temporal resolution) along with running averages of this data with windows of 60, 120, and 180 min. It is noted that for this storm the model produces a two phase, fast then slow recovery phase due to a sudden drop in plasma sheet density during the interval of southward interplanetary magnetic field (IMF). Also, smoothing the input with a window larger than 60 min changes the entire magnetosphere and reduces the plasma sheet density and pressure, therefore a less intense storm develops. It is worth mentioning that the main phase (measured from Storm Sudden Commencement to minimum *Dst*) for this magnetic storm lasted about 3 h. This explains the change in the *Dst* profile for the 120 and 180 min averaged input. Averaging only IMF B_z or solar wind density reveals that all input parameters are important for the development of the storm, but B_z is the most significant. Also, comparison with *Dst* predictions (using the formula of O'Brien and McPherron (2000)) are presented and discussed. For all cases studied, there are no significant differences for Cross Polar Cap Potential (CPCP) in both hemispheres, while the nightside plasma sheet density shows a sharp drop when the input is averaged over 60 min or more. Our results indicate that the magnetosphere responds nonlinearly to the changes in the energy input, suggesting the need for a threshold in the amount of energy transferred to the system in order for the ring current to develop. Further increase of the energy input leads to a saturation limit where the inner magnetosphere response is no longer affected by any additional amount of energy contained within high-frequency oscillations, because the magnetospheric system acts as a low-pass filter on the interplanetary magnetic field.

Citation: Ilie, R., M. W. Liemohn, and A. Ridley (2010), The effect of smoothed solar wind inputs on global modeling results, *J. Geophys. Res.*, *115*, A01213, doi:10.1029/2009JA014443.

1. Introduction

[2] Magnetospheric dynamics are mainly controlled by the two external drivers of the solar wind and the interplanetary magnetic field (IMF). *Dungey* [1961, 1963] was the first to propose that the solar wind energy input into the Earth's magnetosphere is controlled by the solar wind plasma and the IMF, which in turn determines the dayside reconnection rate. The reconnection process is responsible for enhancing the mass and magnetic flux transport from the dayside magnetosphere to the magnetotail when the IMF is southward. During times when the IMF is in the same direction as the geomagnetic field, the plasma convection at high latitudes is more complex, and the transport of magnetic flux can be from the magnetotail to the dayside.

[3] The result of a magnetic storm is the formation of an intense, westward toroidal current that encircles the Earth in the equatorial plane [e.g., *Tsurutani and Gonzalez*, 1997]. This ring current occupies geospace from 2 to 7 Earth radii and is formed through convective transport and drift of ions (mainly H^+ and O^+) in the energy range of 10–200 keV.

[4] While magnetospheric disturbances are highly complex phenomena, it is common practice to use the *Dst* index (disturbance storm time) as a measure of the ring current intensity. The *Dst* index is based on measurements from ground-based magnetometers placed close to the magnetic equator [*Sugiura and Kamei*, 1991] and contains contributions from the magnetopause currents, both partial and symmetric ring current, magnetotail currents along with Earth-induced currents and possibly the substorm current wedge when it is very strong. In spite of being "contaminated" by various current systems, numerous studies [e.g., *Greenspan*

[1]Department of Atmospheric, Oceanic and Space Sciences, University of Michigan, Ann Arbor, Michigan, USA.

0148-0227/10/2009JA014443$09.00

and Hamilton, 2000; *Siscoe et al.*, 2005] showed that the partial and symmetric ring currents are the main contributors to the magnetic perturbation in the horizontal component of the geomagnetic field. Furthermore, throughout the literature, it has been shown that a strong relationship between the variation of the *Dst* index during storms and the energy content of the ring current exists [e.g., *Jorgensen et al.*, 2001; *Liemohn and Kozyra*, 2003].

[5] There are still things we do not know about the storm-time ring current and plasmasphere, especially with regard to the ring current's nonlinear feedback on the energy input. *Ebihara et al.* [2005] suggested that the ring current response is nonlinear with respect to changes in the plasma sheet density, and this might be one factor responsible for the ring current decay. On the other hand, a recent study by *Lavraud and Jordanova* [2007] shows that the proton ring current energy is increasing with increasing plasma sheet density, predicting a linear relationship between the two. *Palmroth et al.* [2003] used global magnetohydrodynamic (MHD) simulations to investigate the solar wind energy transfer to the magnetosphere and found that the during the main phase of the magnetic storm the energy transferred is well correlated to the solar wind parameters while during the recovery phase the correlation is lost. Also, the majority of empirical models that provide a prediction for the *Dst* index are linear with respect to the solar wind parameters [e.g., *Burton et al.*, 1975, *O'Brien and McPherron*, 2000; *Temerin and Li*, 2002, 2006]. Nonlinear dependence on the dynamic solar wind pressure is considered by some models [e.g., *Wang et al.*, 2003], while *Siscoe et al.* [2005] suggested that nonlinearity of the system should be based on the eastward component of the interplanetary electric field, rather than the ram pressure.

[6] There are many mechanisms that are responsible for the particle energization in the inner magnetosphere but the two most important are the ionospheric electric potential and the properties of the near-Earth plasma sheet. The formation of an intense ring current requires significantly high values of both of these drivers [*Liemohn and Kozyra*, 2003], while a decrease in any of them will lower the amount of energy entering the ring current, independent of the nature of the driver [*Kozyra et al.*, 2002; *Liemohn and Kozyra*, 2005].

[7] Transient spikes in the solar wind parameters are observed during most magnetic storm events, leading to considerable changes in the convection strength in the Earth magnetosphere, therefore altering the flow of plasma sheet particles that contribute to the total energy content of the ring current.

[8] A study by *Chen et al.* [1993, 1994] showed that spikes added to the magnetospheric convection produce enhancement of the ring current, because of an increase in diffusive transport of ions with energies over 160 keV. *Ganushkina et al.* [2000, 2001] suggested that the short-lived intense electric fields are responsible for the observed ion flux enhancements inside the plasmapause during storms. Furthermore, inner magnetosphere simulations [*Khazanov et al.*, 2004] using time averages of the electric potential show that temporal resolution higher than 5 min is needed in order to correctly estimate the energization and injection of the high-energy plasma sheet electrons. Similarly, *Ganushkina et al.* [2006] found that the short-lived pulses in the near-Earth electric field had a profound influence on the enhancement of the energetic tail of the ring current ion population.

[9] Conversely, many studies have shown that there is a time delay of few minutes between the time the IMF reaches the magnetopause and the ionosphere starts to react [i.e., *Ridley and Clauer*, 1996; *Ridley et al.*, 1998; *Ruohoniemi and Greenwald*, 1998; *Slinker et al.*, 2001; *Lu et al.*, 2002]. Further, the ionospheric potential takes 10–20 min to fully change from one state to another. *Goldstein et al.* [2003] found that the electric potential response time from solar wind to the inner magnetosphere is around 30 min. *Tsurutani et al.* [1990] describeed the magnetosphere as a low-pass filter, i.e., the existence of a break in the IMF B_z–*AE* coherence spectrum at about 5 h period. Moreover, the statistical study of *Murr and Hughes* [2007] suggests the ionosphere is insensitive to frequencies higher than 0.8 mHz in the IMF, meaning that the magnetosphere-ionosphere system naturally acts as a low-pass filter of the interplanetary magnetic field. Similarly, *Takalo et al.* [2000] showed that the low frequencies in the *AE* index are correlated to the low frequencies in the rectified eastward component of the interplanetary electric field, while the high frequencies are associated with the intrinsic dynamics of the magnetosphere.

[10] The question still remains: If the ring current shows a linear response with respect to its drivers, then the presence of the transient spikes alone in solar wind parameters should have no extra contribution to the energization and loss of the ring current population. Smoothing the solar wind plasma and IMF, therefore reducing the solar wind energy transferred to the magnetosphere, should yield a linear response of the inner magnetosphere with respect to the energy input.

[11] Understanding how the morphology of the plasmasphere and ring current changes as a function of various factors, processes, source terms, and conditions is critical to our understanding of the geospace domain. While in situ measurements of the inner magnetosphere broaden our understanding of the dynamic processes that dominate this region, the energization of the system is still a quite difficult issue to examine using observations alone. Consequently, global magnetohydrodynamic (MHD) simulations provide an excellent alternative for investigating the large-scale coupling of the solar-wind-ionosphere-magnetosphere system, especially when such a model is combined with kinetic physics models from various regions of the space where coupling processes are important (like the inner magnetosphere). The presented work addresses this open issue by examining the event of 22 September 1999 through global magnetosphere simulations within the Space Weather Modeling Framework (SWMF), using a variety of time-averaged solar wind inputs.

2. Space Weather Modeling Framework

[12] The Space Weather Modeling Framework (SWMF) is a robust, high-performance numerical tool that can be used or customized to link together Sun to Earth modeling components, capable of simulating physics from the solar surface to the upper atmosphere of the Earth [*Toth et al.*, 2005]. The SWMF integrates numerical models for numerous physics domains self-consistently solving the physics

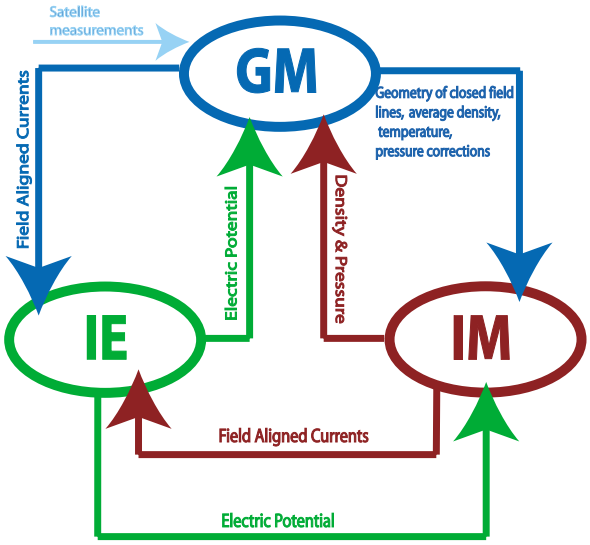

Figure 1. Coupling schematic of the GM-IM-IE coupling within SWMF.

within each region of interest and the coupling between them. This includes models of the solar corona (SC), eruptive event generator (EE), inner heliosphere (IH), solar energetic particles (SP), global magnetosphere (GM), inner magnetosphere (IM), plasmasphere (PS), radiation belt (RB), polar wind (PW), ionosphere electrodynamics (IE), and upper atmosphere (UA) coupled into a complex model. Each domain can be represented with alternative physics models, and the coupling of these modules makes the SWMF a unique and powerful tool in simulations that were not possible with individual physics models. It has been extensively used for scientific studies of the geospace by many authors [i.e., *Toth et al.*, 2007; *Zhang et al.*, 2007; *Yu and Ridley*, 2009]. In the following, we will briefly describe the domains relevant to this study.

[13] The global magnetosphere (GM) domain describes the magnetic field and plasma properties in the outer magnetosphere and encompasses the bow shock, the magnetopause, and the magnetotail of the planet. There is one model for the global magnetosphere in the SWMF, the Block Adaptive Tree Solar-wind-type Roe Upwind Scheme (BATSRUS) global magnetohydrodynamic (MHD) model [*Powell et al.*, 1999; *Gombosi et al.*, 2002; Toth et al. 2006]. This model solves the resistive magnetohydrodynamic equations, everywhere outside an inner boundary near Earth, taken here at 2.5 R_E. In the regions close to the body, where the grid overlaps with that of the Inner Magnetosphere component, the MHD results are nudged toward the IM results. For this study, we used as upstream boundary condition measurements from the ACE spacecraft. An electric potential given by the Ionosphere Electrodynamics component provides the velocity at the inner boundary for the GM domain. The density is set to a fixed value of 28 cm^{-3}, while the temperature and the magnetic field are continuous through the boundary.

[14] The inner magnetosphere (IM) domain consists of the closed field line region, solving the energy-dependent particle flows of hot ions and electrons. The Rice Convection Model (RCM) [*Harel et al.*, 1981; *De Zeeuw et al.*, 2004] is one of the IM models, and it was used for this study. The GM domain provides the RCM outer boundary plasma information along with the closed field line volumes for the IM component, while IM computes the density and pressure along those closed field lines and feeds this information to GM in order to correct these values. Also, for these simulations, all ions are considered to be protons, and charge exchange collisions are not considered within the RCM domain.

[15] Within the ionospheric electrodynamics domain, the two-dimensional electric potential and auroral precipitation patterns are described. The SWMF uses an ionospheric model that is a combination of an electric potential solver and a model of the electron precipitation [*Ridley and Liemohn*, 2002; *Ridley et al.*, 2004], and is needed for proper GM and IM domain simulations. Field-aligned currents are provided by the global magnetosphere domain while IE provides the electric potential to the GM and IM. The field-aligned currents are computed at 3.5 R_E in the magnetosphere and then mapped down into the ionosphere. An illustration of the coupling is presented in Figure 1.

[16] In this study, the inner boundary of GM is set at 2.5 R_E from the center of the Earth where the flows generated by the ionospheric potential are set. The simulation domain is defined by x ranging from [−224 R_E, 32 R_E], with y and z ranging from [−128 R_E, 128 R_E]. The IM domain overlaps with the GM domain and changes according to the open–closed field line boundary information provided by BATSRUS; the IM domain typically extends to 10 R_E in x and y coordinates in the equatorial plane, within the GM region. We ran the model with refined spatial resolution, the smallest being set to 1/8 R_E in the shell region from 2.5 to 3.5 R_E, and close to the Earth (x: 16 R_E, −32 R_E, y: −8 R_E, 8 R_E, z: −8 R_E, 8 R_E) the resolution was set to 1/4 R_E. Close to the tail and bow shock the resolution was set to 1/2 R_E, while everywhere else it was 2 R_E. Coupling the three components enables passing information back and forth between the GM, IE, and IM. The GM and IE components are coupled every 5 s, meaning that the electric potential from IE and the field-aligned currents from the GM are updated at this frequency. The IM-GM and IE-IM couplings were set to 10 s (two time steps in the RCM). The IM obtains the field topology and plasma information from the GM component, while getting the electric potential from the IE and provides the density and pressure corrections back to GM every 10 s. Typically, each simulation domain contains about 2.5 million cells and a BATSRUS time step of 0.7 s (RCM has a 5 s time step). For this particular event, the 10.7 cm solar radio flux (F10.7) was set at 140.1 Jy.

3. Solar Wind Inputs

[17] Solar wind observations from the ACE satellite, orbiting around the Lagrange 1 point on the Sun-Earth line, were used as inputs in the SWMF simulation. Note that the data are propagated from the satellite location to (32, 0, 0) R_E in the geocentric solar magnetospheric (GSM) coordinate system using the Minimum Variance Analysis method of *Weimer et al.* [2003] and *Weimer* [2004].

[18] To assess the role of small-scale fluctuations in the solar wind plasma, we averaged the input data (4 min temporal resolution) with running average windows of 60, 120,

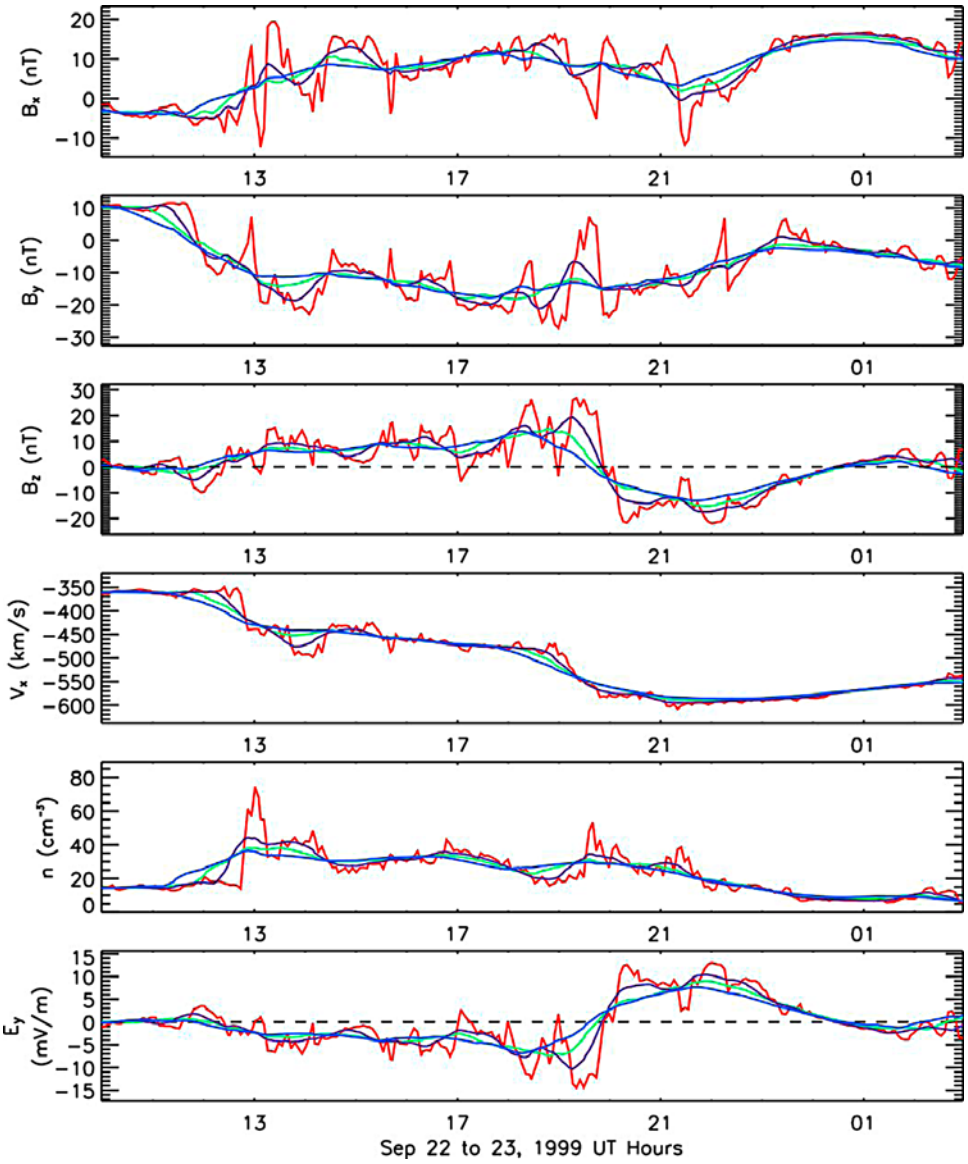

Figure 2. Averaged Inputs for the 22 September 1999 event. Red lines show the ACE observations with a temporal resolution of 4 min, and the running averages with windows of 60 min (purple line), 120 min (green line), 180 min (blue line). From top to bottom are presented the input parameters: B_x (nT), B_y (nT), B_z (nT), v_x (km/s), density (cm^{-3}), and eastward component of the electric field E_y (mV/m). The vertical dashed line in the B_z plot indicates the northward or southward turning of the field.

and 180 min, in this way decreasing the energy input into the magnetosphere. Figure 2 shows solar wind plasma and interplanetary magnetic field (IMF) parameters for the 22 September 1999 event. The different colored lines correspond to different input data: Red lines show the 4 min temporal resolution ACE observations, while purple, green, and blue lines correspond to 60, 120, and 180 min running averages, respectively.

[19] The event chosen for this study is an intense, interplanetary coronal mass ejection (ICME) driven magnetic storm, showing a large disturbance of the geomagnetic field with an observed *Dst* index minimum of −178 nT. A well-defined shock is observed in the solar wind, showing a tremendous increase in solar wind particle density at about 1252 UT, from approximately 15 cm^{-3} to 60 cm^{-3}. The B_z is mostly northward until 1952 UT when it becomes negative and stays negative until 0032 UT on 23 September, with a minimum value of approximately −22 nT. When we smooth the data with a window of 3 h, the shock in solar wind plasma density is not as sharp as before, showing a maximum value of 36.5 cm^{-3}, while the B_z southward turn happens a few minutes earlier than seen in the 4 min data and only reaching a minimum of −13 nT. The X component of the solar wind velocity is one parameter for which the effect of averaging is not as significant, mostly because v_x is quite steady, showing very little temporal variation.

[20] Geomagnetic activity is powered by the solar wind energy injected into the magnetosphere; therefore, we use this quantity as an indication of inner magnetospheric activity. Integration of the rectified eastward component of the inter-

Table 1. Values of the Time-Integrated Energy Input Into the System for Different Simulations and the Percent Difference Between the Energy Input Produced by the 4 min Resolution Input Data and 60, 120, and 180 min Averaged Solar Wind Inputs

Input Resolution	4 min	60 min	120 min	180 min	180 B_z Only	N Only
I (V s/m)	120738	106959	92124	82039	83042	120738
Percent difference	0	12.1	26.9	38.2	36.9	0
Dst (nT)	−265	−254	−131	−42	−138	−201
Percent difference	39.3	35.2	30.4	123.6	25.3	12.1

planetary electric field over the time yields a total energy input into the Earth's magnetosphere, and it is defined as follows:

$$I_{E_y} = \int_{t_1}^{t_2} E^*_{y,\mathrm{sw}} dt, \tag{1}$$

where $E^*_{y,\mathrm{sw}}$ is

$$E^*_{y,\mathrm{sw}} = \begin{cases} 0 & \text{if } B_z \geq 0 \\ (v_x \cdot B_z) & \text{if } B_z < 0, \end{cases} \tag{2}$$

and t_1 corresponds to the start time of the simulation (22 September 1000 UT), while t_2 is the end time of the simulation (23 September 0300 UT). Note that E_y for all cases was computed using the smoothed values of v_x and B_z and not by smoothing the high-resolution E_y time series.

[21] Percent differences were calculated between energy input when the temporal resolution of the upstream solar wind was 4 min and energy input for the 60, 120, and 180 min averaging of the data and shown in Table 1, the first two rows. The smoothing of the data cuts the power input into the system by about 38%, when the averaging is done with a window of 3 h. It is worth mentioning that the bulk of the energy input is transferred during the storm main phase (from 2000 UT to 2300 UT), therefore including the quiet time in our integration of E_y does not change its value significantly (not shown here). Rows 3 and 4 show the simulated *Dst* index values and percent differences between the observed value and the ones produced by our simulations. We note that the 180 min smooth-density-only run produces a ring current closest to the observations, while the 3 h smooth data produce the weakest *Dst* index.

4. Smoothing All Input Parameters

4.1. Magnetospheric Response

[22] The *Dst* index results are shown in Figure 3 for all cases. The modeled *Dst* index is calculated by solving the Biot-Savart integral for all the electric currents encompassed by the BATSRUS simulation domain from the inner boundary, and taking the magnetic field disturbance along the z axis. Again, the colored lines show the results from the four different temporal resolution inputs: 4 min (red), 60 min (purple), 120 min (green), and 180 min (blue), while the black dashed line shows the observed *Dst*, and the black continuous line corresponds to the SYM-H index. The comparison with the observed indices provides us with a measure of the ability of the model to accurately represent the inner magnetospheric response. The 60, 120, and 180 min averaging runs were started from the same common restart file (obtained from the 120 min run) just before 1800 UT as opposed to 1000 UT for the case of 4 min averaging. The reasoning behind this was to use less computer resources, and it was motivated by the fact that this time was still several hours before the main phase of the storm (during the very quiet pre-storm interval).

[23] We see that when the 4 min and 60 min temporal resolution is used in our simulation, the modeled *Dst* profiles

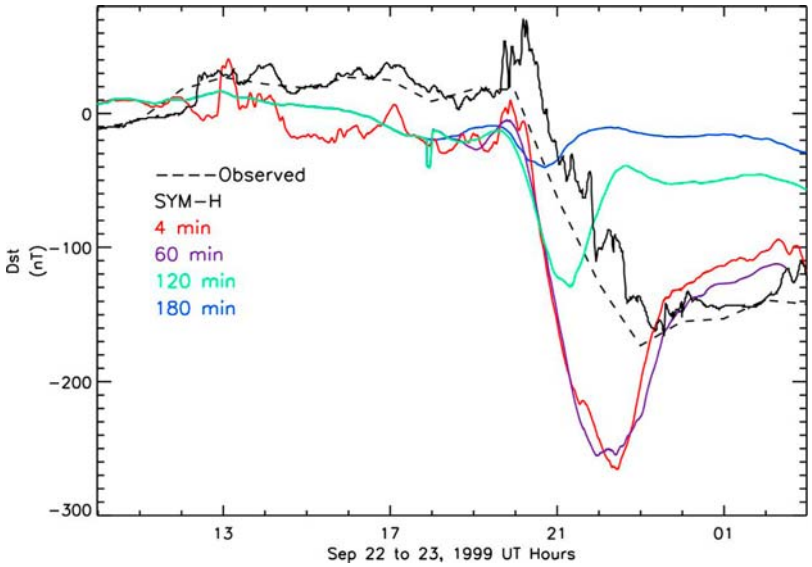

Figure 3. *Dst* index simulation results for all the runs using averaged inputs for the 22 September 1999 magnetic storm. Each colored line corresponds to different simulation results using different time resolution input data: 4 min (red line), 60 min (purple line), 120 min (green line), 180 min (blue line). The black dashed line shows the observe *Dst* index, while the black continuous line corresponds to the SYM-H observations.

are quite similar, peaking within the same hour and dropping to about the same value, then recovering very fast during the first 2 h and slower after that. For both of these cases, the simulated *Dst* index is dropping sooner and lower (more intense) than the observed value, indicating a stronger ring current and a shift in the peak of the storm. It is worth mentioning that smoothing the input with a window of 1 h does not make a significant difference in the *Dst* profile.

[24] For the case when the inputs are smoothed with a window of 2 h, the *Dst* index is less negative (less intense) than the observed one, recovers quickly for 2 h and after that the recovery is slow, as noted in the previous cases as well. Similar behavior is seen in the case of the simulation that used *Kp*-like (3 h) averaged data, only this time the *Dst* index did not go below −40 nT. Please note that the main phase of the 22 September 1999 event only lasted about 3 h; therefore averaging over 180 min, the B_z southward magnitude has been greatly decreased, implying that the magnetic convection will be significantly weaker.

[25] Interestingly enough, for all cases, the *Dst* profile showcases a two-phase recovery. There are a few hypotheses that are trying to explain this fast and then slow-recovery phase. *Liemohn et al.* [1999] postulated from numerical simulation results that the fast-early-recovery phase is due to particle flow out of the inner magnetosphere toward the dayside magnetosphere. Also, *Jorgensen et al.* [2001] suggested that different processes are responsible for the fast- and the slow-recovery phase, that is, during the early fast recovery the lifetime of trapped ring current particles is considerably shorter compared with the late-slow-recovery phase.

[26] Many authors [e.g., *Liemohn et al.*, 1999, 2001; *Jordanova et al.*, 2003] argued that charge exchange processes are primarily responsible for the decay of the ring current during the late-recovery phase, because of the reaction's slow timescale compared with the loss of ions to the dayside due to large-scale plasma convection. In our study, we cannot conclude anything about the charge exchange losses since these losses are not explicitly included into our global magnetospheric simulations. Yet, our simulation results suggest that such behavior is reproducible without the charge exchange mechanism explicitly taken into account.

[27] Figure 4 presents the BATSRUS pressure distribution in the *X*–*Y* plane (as modified by the RCM) during the development of the storm, for all our simulation runs. Pressure is directly correlated with the current density and provides a good measure of the current distribution. The ring current develops at different times (UT) during the storm, depending on the averaging window, with the least intense value of the *Dst* index occurring during the 3 h averaged input with a ring current that grows and peaks sooner. In the 4, 60, and 120 min averaged inputs runs, the current becomes symmetric around 2300 UT (weaker in the latter case), while for the 180 min averaged inputs run, pressure is close to one order of magnitude lower, resulting in a less-disturbed geomagnetic field (as seen in Figure 3). In the last column of Figure 4, the plasma sheet is very weak, while in the first two columns, the plasma sheet shows an intensification during the main phase and decays close to 2400 UT, at the same time as the start of the slow-recovery phase. Similar features are seen in the case of 120 min averages; the drop in the near Earth plasma sheet pressure is followed by the slow recovery of the ring current. While the *Dst* decay is mainly modulated by the ring current, the recovery is controlled by both the ring and the tail current systems [*Feldstein et al.*, 2000]. A rapid decay of the tail current can cause a sudden recovery in the *Dst* index. On the other hand, *Ohtani et al.* [2001] argued that the contribution of the tail current to the *Dst* is approximately 20%–25% of the total. So far it is worth considering that the two-phase decay seen in the *Dst* index might not be due only to the loss of trapped ring current energy, but also to the early decay of the tail current system.

4.2. Midnight Plasma Sheet

[28] The major sources for the ring current population are the ionospheric outflow and the injection of the plasma sheet particle into the inner magnetosphere. Plasma sheet particles are accelerated due to the convection electric fields and become trapped and start gradient-curvature drifting around the Earth, forming the ring current. Therefore, we investigate the contribution of the plasma sheet density to the energization of the ring current. To do so, we have included 24 virtual satellites in our simulations located 1 h of local time apart at the geosynchronous orbit and extracted values throughout the simulations. Our model solves the MHD equations for the mass density, and it provided us with a measure of plasma sheet population expressed in atomic mass units per cubic centimeter (amu/cm^{-3}). Since compositional information is not available, in order to convert it to number density expressed in units of particles per cubic centimeter, we are using the formulae of *Young et al.* [1982], that is, empirical relationships between the densities of O^+ and H^+ as a function of *Kp* index and the solar flux F10.7, as described below:

$$n(O^+) = 0.011 \exp(0.24Kp + 0.011F10.7) \tag{3}$$

$$\frac{n(O^+)}{n(H^+)} = 0.045 \exp(0.17Kp + 0.010F10.7). \tag{4}$$

[29] The density provided by our model (n_{SWMF}) was corrected in such a way that accounts for the percentage of both oxygen and hydrogen ions:

$$n_{corrected} = n_{SWMF} \frac{n(H^+) + n(O^+)}{n(H^+) + 16n(O^+)}. \tag{5}$$

[30] Note that for this event, *Kp* was fluctuating between 2 and 8, with a maximum of 8 at the storm peak.

[31] Figure 5 presents the geosynchronous nightside plasma sheet density (averaged over the whole nightside), the radial component of the bulk velocity, and the sunward particle flux results for 4 min temporal resolution and 3 h averaged solar wind input cases only, used in our study. The radial velocity and the density were averaged across the nightside around the geosynchronous orbit, from 18 LT to 06 LT. For the case of the high-resolution solar wind input (the red line in Figure 5), both the plasma sheet density and the sunward velocity are steady up until 2000 UT, at which time B_z becomes negative, and the plasma sheet density increases and remains at elevated values for most of the duration of the main phase. The radial velocity is considerably

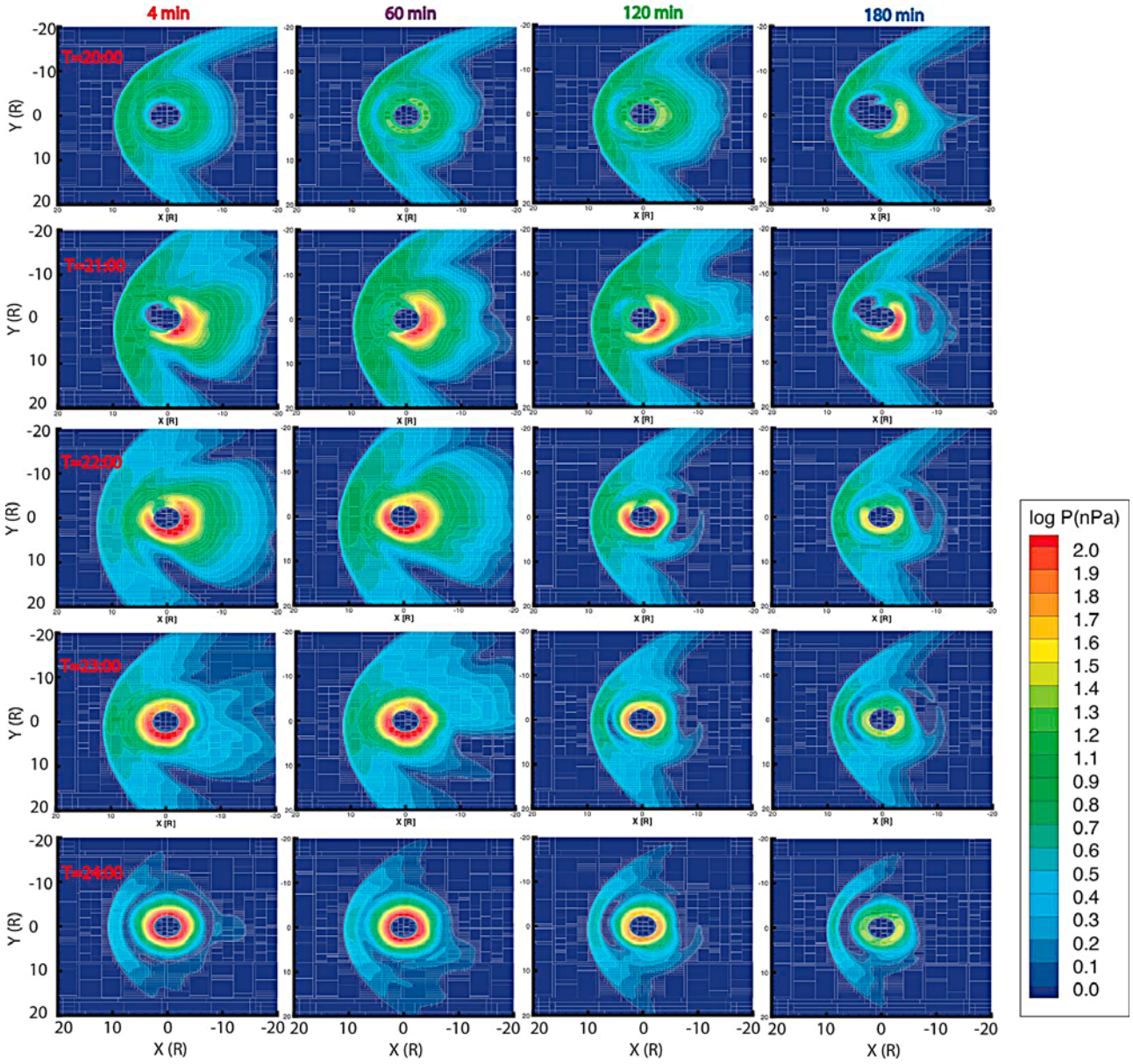

Figure 4. Pressure distribution in the *X*–*Y* plane for all simulation results. From left to right, each column corresponds to a case study: 4 min, 60 min, 120 min, and 180 min running averages of input parameters. From top to bottom, we present snapshots of the pressure on a logarithmic scale at five times during the event: 2000–2400 UT on 22 September 1999. The scale of the plot is logarithmic (base 10) and is expressed in nPa.

enhanced, reaching a maximum of about 80 km/s for the 4 min simulation while the 3 h averaged input (the blue line in Figure 5) yields a maximum velocity of under 30 km/s. Interestingly, we note a sudden drop in the nightside plasma sheet density just before the storm maximum, from about 4 cm^{-3} to approximately 2 cm^{-3} (the red line in Figure 5). Similarly, the sunward velocity for the high-resolution input data is increasing considerably closer to the storm maximum (2200 UT) only to decrease just before 0000 UT, at the same time with the start of the slow-recovery phase. Therefore, it is suggested that fewer plasma sheet particles are accelerated enough to gain access to the inner magnetosphere and become trapped. The difference in the earthward particle flux for the two cases is significant. Smoothing the input with a window of 3 h yields a steady, less-dense plasma sheet density on the nightside, along with weaker flux and lower radial velocity. Therefore, removing the transient spikes in the solar wind by smoothing the solar wind input data with a window of 3 h yields a less-dense and less-energetic plasma sheet population.

[32] The density drop might explain the rapid recovery of the ring current, since the source of particles is depleted, and there are very few additional particles injected into the ring current. Smoothing the input with a 3 h window produces a steady, low-density plasma sheet, showing very little variability. Again, this is explained by the fact that the weak

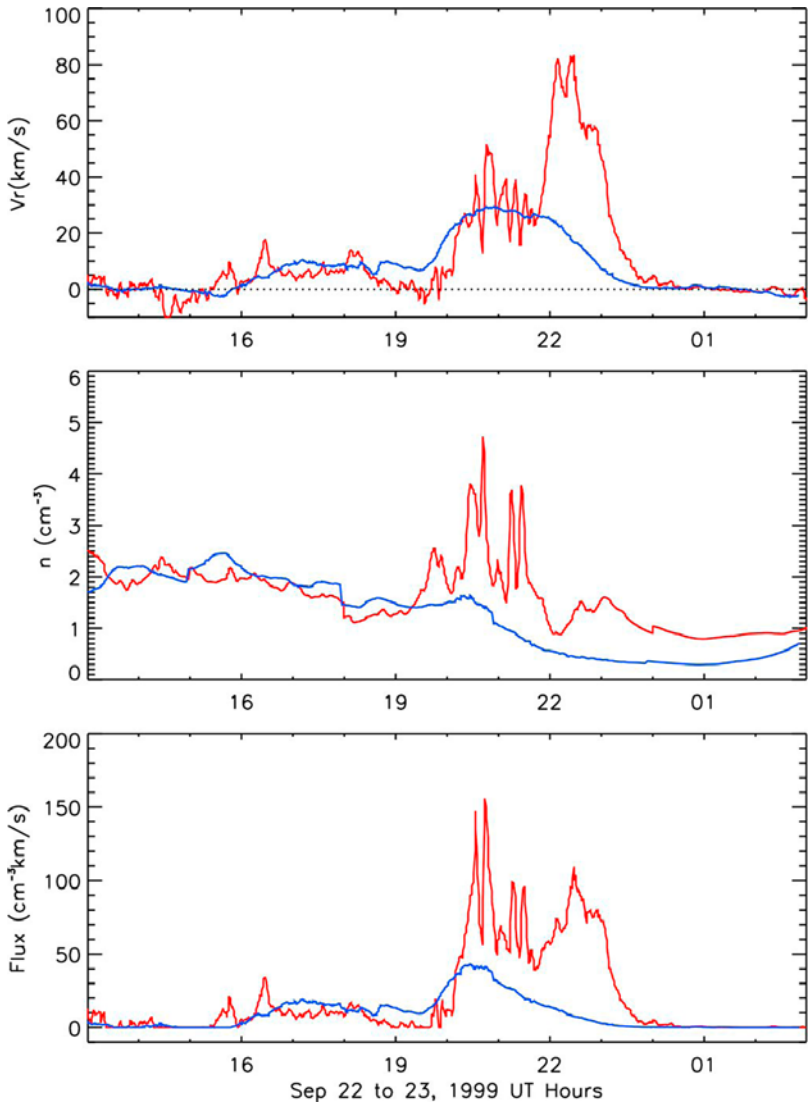

Figure 5. (middle) Nightside average of plasma sheet density extracted at the geosynchronous orbit, (top) radial velocity, and (bottom) particle flux results for the 4 min (red line) and 180 min (blue line) averaged solar wind inputs.

and smooth southward IMF B_z (as shown in Figure 2, the blue line in the third plot from top) decreases the magnetospheric convection and produces a less variable plasma sheet.

[33] A study by *Takahashi et al.* [1990] shows that both particle energy and the length of recovery of the cross tail potential are controlling the amount of plasma trapped on closed field lines. These authors propose that the recovery of the *Dst* index is due to a combination of decreased injection and charge exchange of trapped particles. Moreover, they show that the drop in the plasma sheet density during the early-recovery phase is the main contributor to the fast recovery of the simulated ring current. In addition, the late slow recovery occurs when the IMF B_z becomes positive. The particle injection rate is strongly dependent on the cross tail potential difference, and therefore the variation in the IMF B_z controls this potential. *Liemohn et al.* [1999] used computer simulations to examine two distinct events, one during solar minimum and one during solar maximum, considering the different oxygen contents during the stormtime injections. They found that the drift losses out to the dayside magnetopause are the major loss mechanism during the main phase of the storms. Their study strengthens the belief that the fast early decay of the ring current is dominated by the "flow out" effect and not by the collisional losses. *Kozyra et al.* [1998a, 1998b] also showed that the ion drift to the compressed dayside magnetosphere is the main loss mechanism that accounts for the fast recovery of the *Dst* index. Moreover, *Liemohn et al.* [2001] stated that changes in the inner magnetosphere plasma sheet density alter the particle open drift paths, and in the case of steady convection, an increase (decrease) in the plasma sheet density produces a more (less)-disturbed *Dst* index. A decrease in the cross tail potential will produce a more symmetric ring current that dominates the induced perturbance in the geomagnetic field.

[34] Our findings are also indicative of the fact that the drop in the midnight plasma sheet density (seen in the higher temporal resolution of the solar wind input runs) controls the

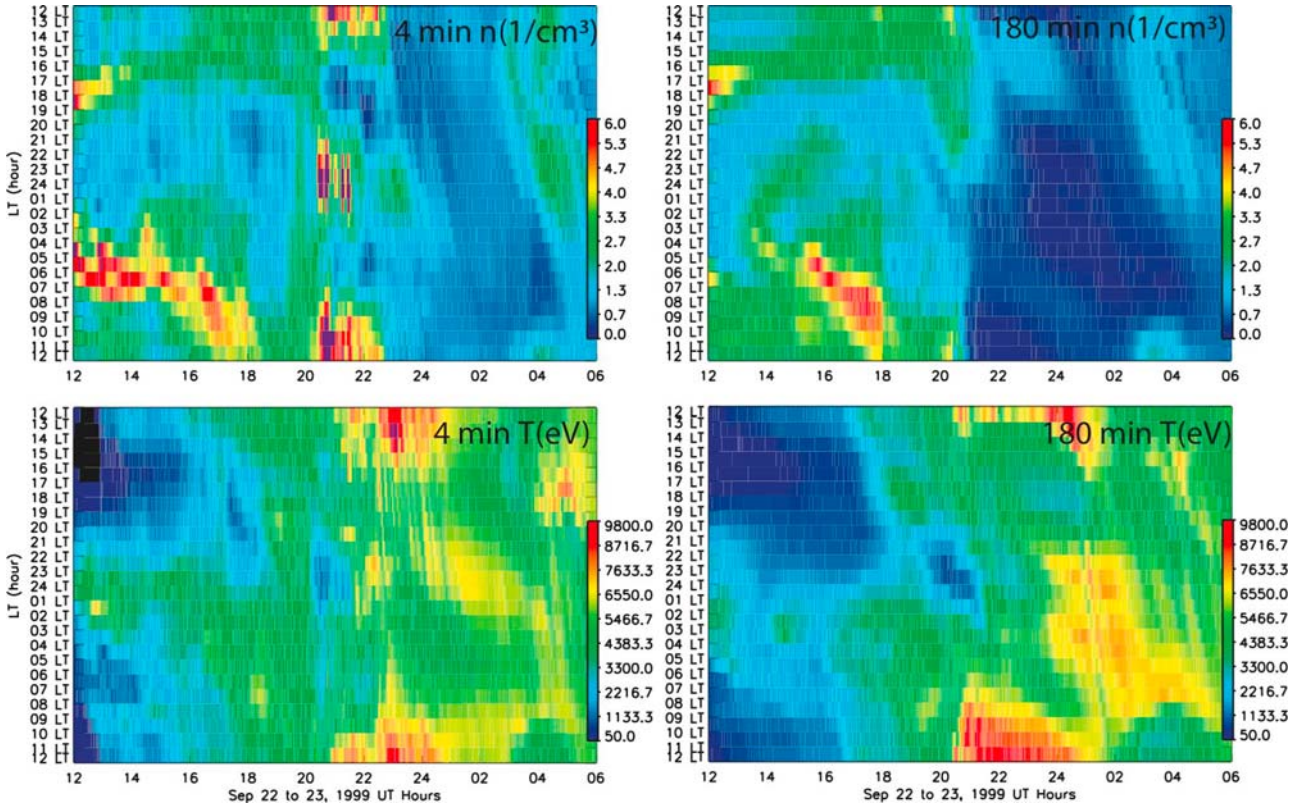

Figure 6. (top) LT-UT map of the density and (bottom) temperature for the (left) 4 min averages and (right) 180 min averages of the input parameters simulation results. Data were extracted from the virtual satellites included in the simulations at geosynchronous orbit.

beginning of the fast-recovery phase, since the fast recovery appears to start at the time the plasma sheet density drops considerably. Also, the time when the Z component of the IMF becomes positive corresponds to the time when the ring current decay becomes slow.

[35] The question still lingers: What causes the sudden loss of plasma sheet particles at the storm maximum, and what mechanisms are responsible for this? Are the small timescale fluctuations in the solar wind responsible for this sudden decay of the ring current or is it just an artifact of the computer simulation?

[36] Figure 6 shows the distribution of density and temperature at the geosynchronous orbit, extracted from the virtual satellites locations, as a function of local and universal time. Once again, the density is corrected as previously described. The black bins indicate values lower than the minimum, while the purple bins indicate values greater than the maximum.

[37] For the 4 min case (top left), the density increases from the dayside to the nightside and shows enhancements at midnight, and at the dayside, during the main phase of the storm. These features are lost when the upstream solar wind input is smoothed with a window of 3 h (top right). The density profiles for both cases have very similar behaviors in the 1200–1800 UT time range. Please note that up to 1800 UT, the density and temperature profiles for the 3 h input data run were obtained from the 120 min averaged input data, since the 180 min run was restarted from about 1800 UT as previously stated. Therefore, the change in density after this time, which corresponds to the actual main phase of the storm, is what interests us. During the recovery phase, the 3 h input produces a significantly lower density in the inner magnetosphere. The particle temperature is enhanced in the morning-afternoon sector for both cases, but the low temporal resolution input (bottom right) reveals an injection of a more energetic particle population on the dawnside, although the density is low. The lower temperatures during this time period throughout the inner magnetosphere are due to the lowered energy input into the system. We note that for both cases, on the nightside, the density is low, and the temperature is enhanced during the recovery phase. The dense midnight plasma just before the peak of the storm (2200 UT) has quite a low temperature, while the dayside counterpart at the same universal time is made up of more energetic particles. Also the dawnside shows a larger depleted density region than the dusk side. Statistical studies [e.g., *Denton et al.*, 2005; *Lavraud et al.*, 2006] reported on the dawn-dusk local time asymmetries. The authors showed that during the main phase of magnetic storms, a time when both convection and ring current strength are high, the plasma density is enhanced primarily in the dawn region. Moreover, cold dense plasma is observed in the midnight sector, mainly during time periods of northward IMF and associated with a cold dense plasma sheet. Our results also indicate the presence of a cold and dense particle population at dawnside during the main phase

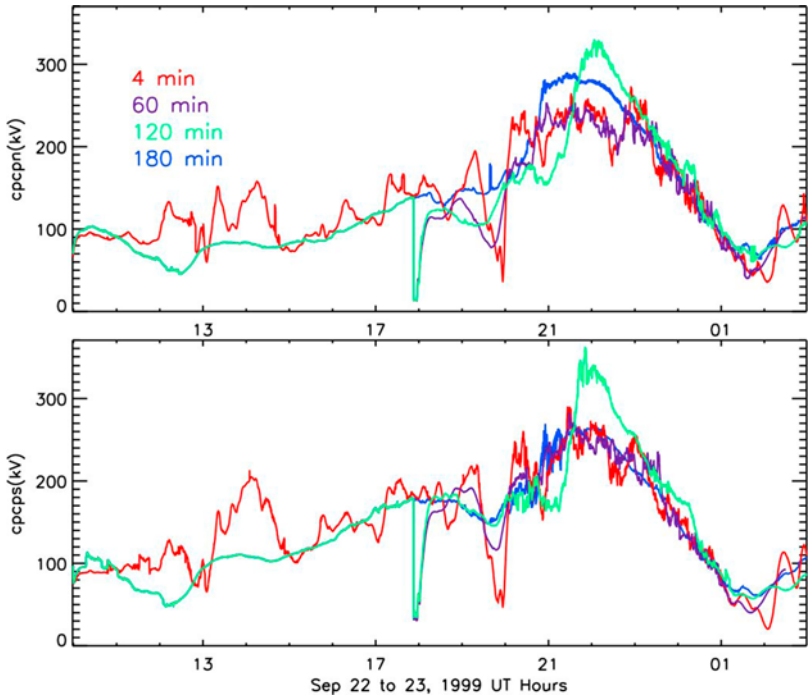

Figure 7. Cross polar cap potential simulation results in the (top) northern and (bottom) southern hemisphere, for all the runs using averaged inputs for the 22 September 1999 magnetic storm. Each colored line corresponds to different simulation results using different time resolution input data: 4 min (red line), 60 min (purple line), 120 min (green line), 180 min (blue line).

of the September 1999 event. Although the midnight dense and low-temperature plasma seen in our high-resolution input run occurs during a period of southward IMF, it is because it takes some time for the cold and dense plasma sheet to convect inward during northward IMF but can rapidly move in the inner magnetosphere when the IMF turns southward.

4.3. Ionospheric Response

[38] Because of the fact that the magnetic field lines of the inner magnetosphere pass through the midlatitude ionosphere, the convection patterns and the cross polar cap potential (CPCP) provide a great proxy to evaluate the ring current dynamics.

[39] Figure 7 presents the variations in the cross polar cap potentials in both southern and northern hemisphere predicted by our model over the course of 22 September 1999 magnetic storm. Again, the different colored lines correspond to different simulation results using the averaged solar wind input. It is interesting to note that the 120 min temporal resolution run produced the highest peak potential for this interval. Nevertheless, we can see that for all cases, the cross polar cap potential has a very similar behavior. This is indicative of the fact that the small timescale fluctuations in the solar wind parameters do not appear to affect the cross polar cap potential, and so the flow generated by the change in transpolar potential is not altered significantly by the input averaging.

[40] Since the ionospheric convection strength remained approximately constant in all of the simulated cases, the nightside plasma sheet density is the main parameter that controls the differences in the intensity of the simulated ring current. The loss of ring current particles is due to the lower-density plasma moving to lower-radial distances along the open drift paths. The role of the temporal variations in the nightside plasma sheet inflow in developing a two-phase decay of the ring current is also assessed by *Jordanova et al.* [2003]. Their study concluded that the fast early recovery of the *Dst* is correlated with the sudden drop in the midnight plasma sheet density. Moreover, the two-phase recovery phase results are consistent with the findings of *Liemohn and Kozyra* [2005]. In their numerical study, the two-phase decay of the ring current energy was found to occur when the plasma sheet density was suddenly reduced while the ionospheric convection was kept constant for few hours after the density drop. Suddenly reducing both ionospheric convection and plasma sheet density or just decreasing the convection first and then the density produced a one-phase recovery profile.

[41] Since, in our simulations, we do not include charge exchange processes that are believed to be the ones responsible for the slow decay of the ring current, we attribute the slow-decay phase to the fact that the source of the ring current particles is completely depleted, and along with weaker magnetospheric convection, fewer particles are accelerated (at a less rapid rate) and moved inward to become part of the ring current.

5. Smoothing Selective Input Parameters: B_z and N

[42] Averaging all the input parameters might not give us enough information to quantify which of them is primarily responsible for the decay of ring current. To gain insight into this issue, we smoothed only one parameter at a time:

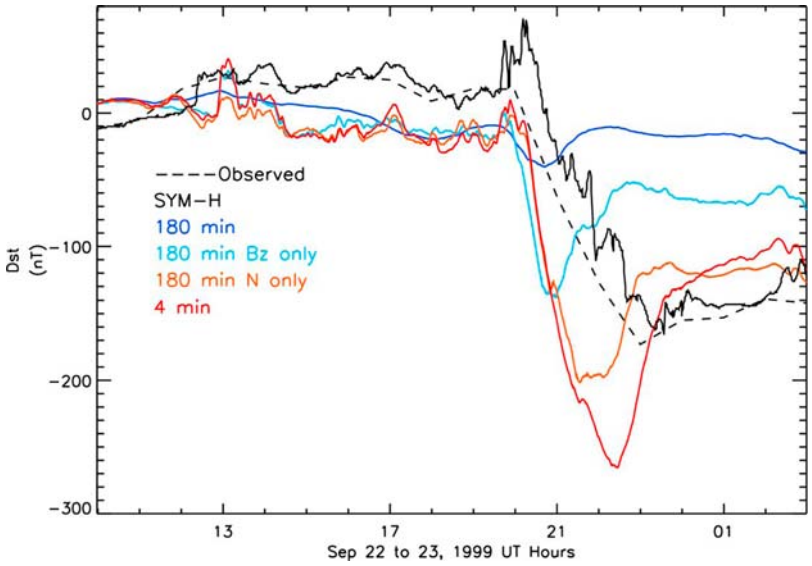

Figure 8. *Dst* index simulation results for the runs using averaged B_z only (light blue line), N only (orange line), 4 min (red line), and 3 h averaging of all inputs (blue line) for the 22 September 1999 magnetic storm. Observed Sym-H and *Dst* indices are shown in black, and black dashed lines, respectively.

In the first case study, we smooth only the Z component of the IMF with a window of 3 h and keep all the others parameters at 4 min temporal resolution, and in the second, we only smooth the solar wind density. The choice of 3 h averaging seemed reasonable since it showed the most drastic response in the development of the storm. In the former case, the energy input changes only by 1.2% from the 180 min energy input and 36.9% from the 4 min one, while in the latter, the energy input is the same as in the case of 4 min averages (since E_y only depends on v_x and B_z).

[43] The effect of smoothing only the B_z and density is shown in Figure 8. The *Dst* profile for the first case is similar with the one for which the input was averaged with a window of 2 h. *Dst* minimum in this case is −138 nT. For this case, the ring current shows more intensification that in the case when all input parameters are averaged over a 3 h window. Even though the amount of solar wind energy transferred to the magnetosphere is not significantly higher, the response of the magnetosphere is definitely greater. Therefore, together all other seven parameters (v_x, v_y, v_z, B_x, B_y, density, and temperature) that constitute the input for our model have a considerable contribution to the energization of the ring current. On the other hand, when we only average density, the *Dst* index drops even lower, peaking at −201 nT, though still higher than in the case of 4 and 60 min averages. These results show us that both IMF B_z and the solar wind density control the energization of the ring current in the SWMF simulations, but the IMF B_z carries most of the contribution.

[44] Looking at the midnight plasma sheet populations (Figure 9), the density from the smoothed-B_z-only run peaks first, but this time delay seems to be due to the fact that the 3 h averaged B_z drops a few minutes before the 4 min temporal resolution IMF B_z. Therefore, this is an artifact of the averaging. Nevertheless, in both cases, we note the increase during the main phase and the sharp drop just before the slow recovery starts, although the size of the peak is larger for the N only run. The sunward velocity for the smoothed-density-only run is similar to the 4 min resolution run, but the peak in velocity in the former case is considerably lower. The velocity profile for smoothed-B_z-only run is similar to the case of 3 h averaged input run. This is indicative of the fact that the Z component of the IMF is the main parameter that controls the particle injection rate. The time the near-Earth tail sunward particle flux starts to decay is well correlated with the start time of the slow-recovery phase.

[45] Snapshots of the pressure distribution at five different times during the storm (Figure 10) also reveal that when only smoothing the solar wind density, a stronger ring current develops along with a greatly enhanced tail plasma sheet pressure. For the case when only the density is smoothed, the tail plasma sheet pressure starts reducing in intensity at about 2300 UT, the same time as when rate of decay of *Dst* index becomes less steep. Similar but less distinct features (since the tail plasma sheet pressure seems to be lower) are seen in the case of only smoothing the B_z.

6. In Situ Data-Model Comparison

[46] During this event, the trajectories of the Geostationary Operations Environmental Satellite GOES 8 and GOES 10 were included in the SWMF simulations, and MHD parameters were extracted along these orbit paths. The magnetic field simulation results are compared to fluxgate magnetometer measurements aboard these satellites and presented in Figures 11 and 12. The satellite trajectories are shown in the top two plots (the black disk shows the location of the inner boundary, in our case 2.5 R_E), followed by the magnetic field components B_x (nT), B_y (nT), and B_z (nT). Please note that the data are in GSM coordinates and the Sun is on the right. A diamond, an asterisk, and a triangle are used to illustrate three sample data points both in the trajectory plots (spacecraft location) and in the magnetic field panels. In all three plots, the black lines show the satellite measurements

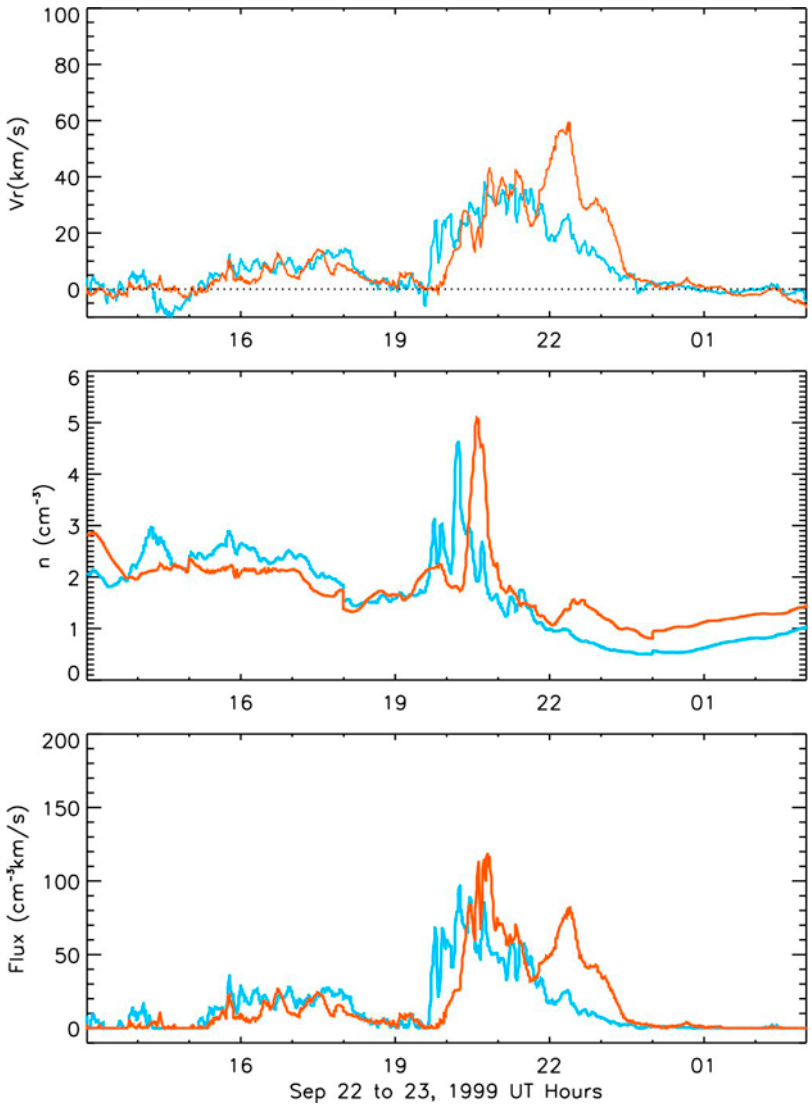

Figure 9. Nightside average of (top) plasma sheet density, (middle) radial velocity, and (bottom) particle flux results for the B_z-only (light blue line) and density-only (orange line) averaged solar wind inputs, extracted at geosynchronous orbit.

while the red and blue lines correspond to model runs using 4 min and 180 min averaged solar wind input, respectively. Figure 11 displays the results from GOES 8. We note that for this event, the spacecraft is located on the dayside at the storm peak (2300 UT). For the case of high-resolution solar wind input, the magnetic field measurements are reproduced remarkably well, with excellent agreement with respect to overall trends, but there are several discrepancies in the details. The smooth rotation in the Y component of the magnetic field is well reproduced by our model, a feature that is lost when the input is smoothed with a window of 3 h. In this case, the magnetic field topology changes greatly, revealing a magnetic field that is less stretched, which in turn is correlated to a weaker ring current. For both simulated cases, B_x is underestimated, while the other two components of magnetic field vector are overestimated during the main phase of the storm.

[47] Similar to Figure 11, Figure 12 shows the magnetic field results for the GOES 10 satellite. In this case too, the spacecraft was located on the dayside during the storm peak. A sharp drop in B_z is observed in the GOES 10 data at about 2000 UT that is very well replicated in our 4 min resolution simulation, while the coarser input data fail to completely capture this feature. Similarly, the large-scale features of B_y are considerably better represented by the high-resolution run. The X component of the magnetic field is again underestimated during the main phase of the storm and even the large-scale features are not well represented for both cases.

[48] At 2100 UT GOES 10 goes out of the magnetosphere. In the 4 min run, this sudden compression of the magnetosphere is well modeled, while in the 3 h run the satellite comes close to the magnetopause but never crosses it.

[49] We note that considerably reducing the energy input into the magnetosphere by removing the transient spikes in the solar wind also has the effect of changing the magnetic

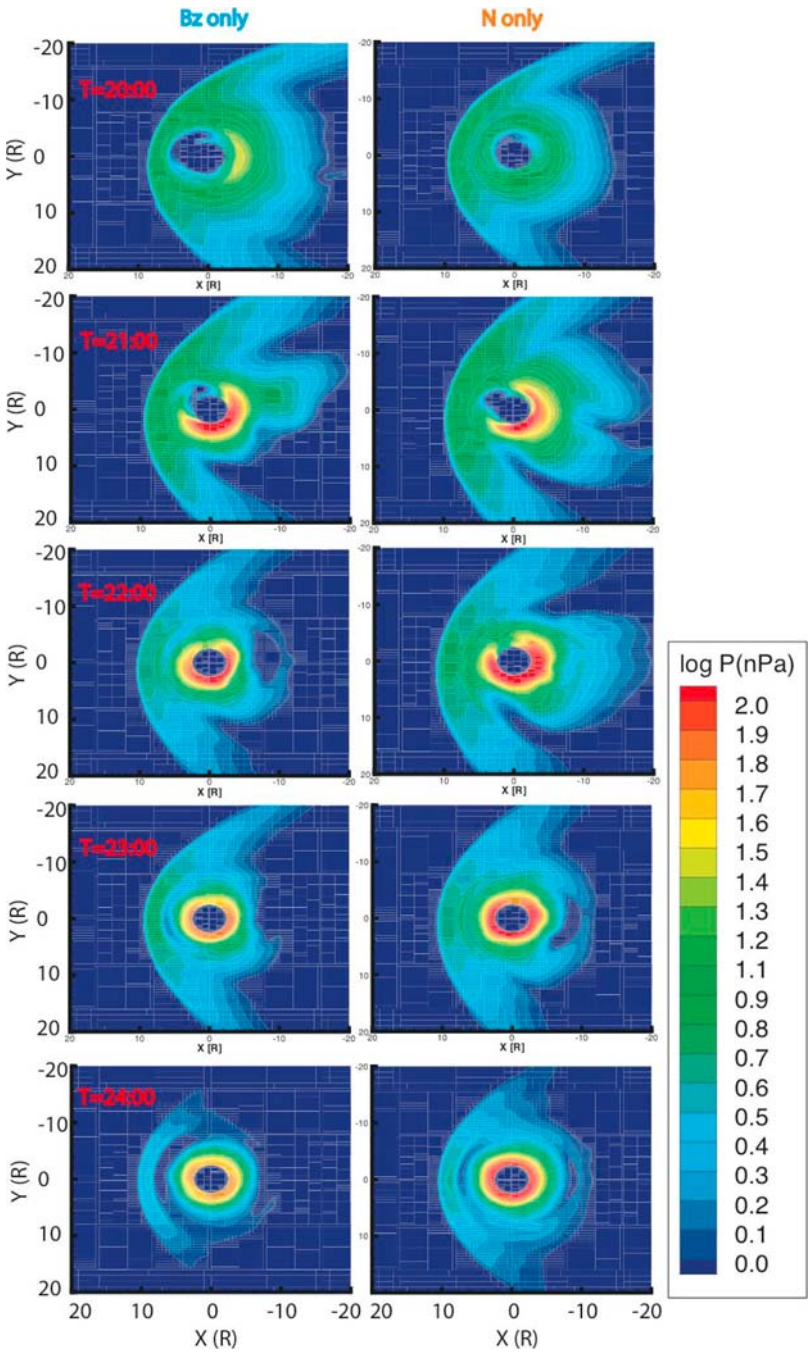

Figure 10. Pressure distribution in the *X*–*Y* plane for all simulation results corresponding to a case study: (left) B_z only and (right) *N* only 180 min running averages of input parameters. From top to bottom, we present snapshots of the pressure on a logarithmic scale at five times during the event: 2000–2400 UT on 22 September 1999.

field topology. This, in turn, alters the particle energies and trajectories while influencing the particle loss rate.

7. Comparison With the Empirical Model

[50] The geomagnetic effectiveness of the solar wind is a complex problem. Predicting the inner magnetosphere response, i.e., of the *Dst* index, from the solar wind parameters has been extensively investigated, and it is usually done by assuming the energy input rate is balanced by an empirical ring current loss rate. Most of the energy input functions are dependent on the southward component of the IMF and the solar wind velocity. Such a global energy balance model is the one of *O'Brien and McPherron* [2000] that determined an empirical expression for the *Dst* index, relating the evolution of this geophysical activity parameter to the solar wind:

$$\frac{dD^*_{\mathrm{st}}}{dt} = Q(t) - \frac{D^*_{\mathrm{st}}(t)}{\tau}, \tag{6}$$

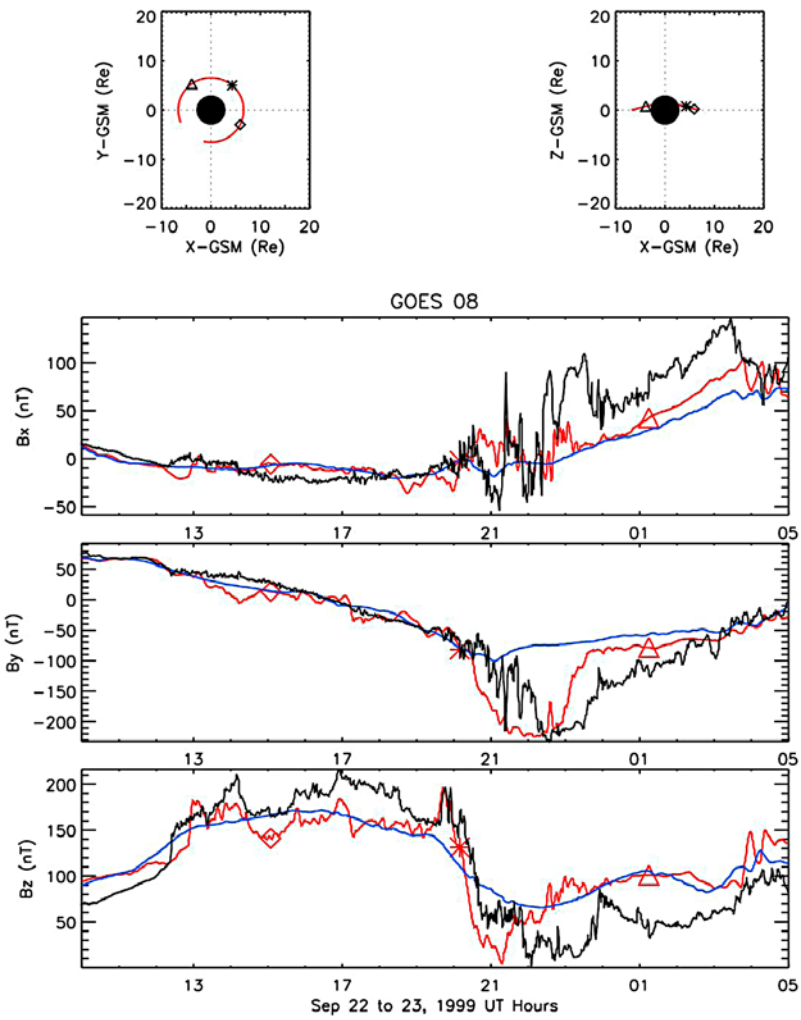

Figure 11. Magnetic field components at the GOES 8 satellite. First and second plots show the satellite trajectory, while the rest show each component of the magnetic field in nT. Each colored line corresponds to different simulation results using different time resolution input data: 4 min (red line) and 180 min (blue line). The black line shows the observations.

where τ represents the decay time of the ring current and is a function of the interplanetary electric field:

$$\tau = 2.4^{*} \exp 9.74/(4.69 + |v_x B_z|) \quad (7)$$

only for negative B_z. The injection function Q is a linear function of the interplanetary electric field:

$$Q(\mathrm{nT/h}) = \begin{cases} \alpha\left(E^{*}_{y,\mathrm{sw}} - E_c\right) & \text{if } E^{*}_{y,\mathrm{sw}} > E_c \\ 0 & \text{if } E^{*}_{y,\mathrm{sw}} < E_c, \end{cases}$$

where $\alpha = -4.4$ nT/h $(\mathrm{mV/m})^{-1}$, $E_c = 0.49$ mV/m. $E^{*}_{y,\mathrm{sw}}$ represents the energy input function and depends on the strength and the direction of the interplanetary magnetic field and the X component of the solar wind velocity. The contribution of the ring current, that is, D^{*}_{st}, is calculated by removing from the *Dst* index the contributions from the magnetopause current along with the diamagnetic effects:

$$D^{*}_{\mathrm{st}} = D_{\mathrm{st}} - 7.26\sqrt{P_{\mathrm{sw}}} + 11 \text{ nT} \quad (8)$$

where P_{sw} represents the solar wind dynamic pressure in nPa. We use this formulation to investigate how well the physics of the storm is represented in our model relative to the empirically based predictions of D^{*}_{st} for this event, for all the solar wind inputs.

[51] Figure 13 shows the *Dst* index predicted by the *O'Brien and McPherron* [2000] empirical formulae (equation (6)). The colored lines show the predicted *Dst* profile using the four different temporal resolution inputs: 4 min (red), 60 min (purple), 120 min (green), and 180 min (blue). The black dashed line shows the observed 1 h resolution *Dst*, while the black continuous line corresponds to the measured 1 min temporal resolution SYM-H index. For this event, minimum *Dst* reached −178 nT, while the SYM-H minimum value was −166 nT. The predicted *Dst* profiles show a linear trend, that is, less solar wind energy input produces less geomagnetic disturbance. The main phase of the storm is quite well reproduced, although the predicted *Dst* shows a slower decrease rate compared to the observed profile. Nevertheless, the start time of *Dst* decay is well captured in the empirical model results. We see that the

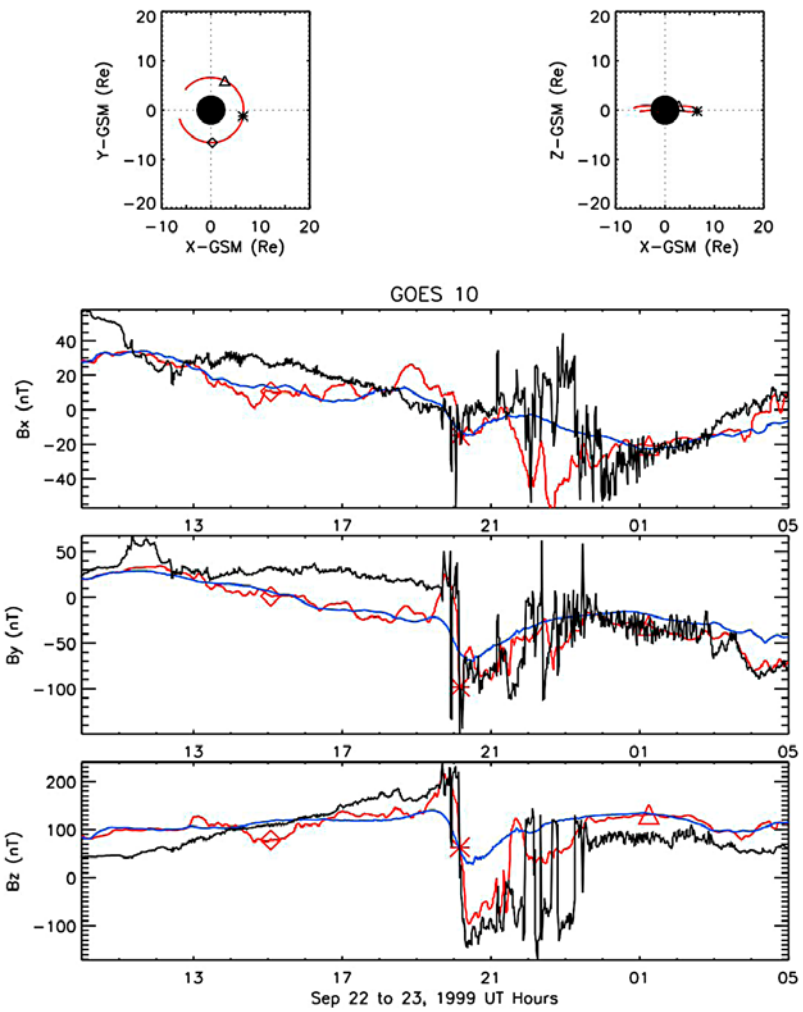

Figure 12. Magnetic field components at the GOES 10 satellite. The first and second plots show the satellite trajectory, while the bottom three plots show each component of the magnetic field in nT. Each colored line corresponds to different simulation results using different time resolution input data: 4 min (red line) and 180 min (blue line). The black line shows the observations.

observed recovery phase of the ring current is faster than that predicted by the *O'Brien and McPherron* [2000] model. We note that the rate of decrease of the predicted *Dst* is increasing with increasing energy input, and the 4 min input data predict a rate of ring current decay closest to the observations. Since the injection function Q as described by *O'Brien and McPherron* [2000] is a linear function of E_y, therefore limited to only v_x and IMF B_z (equation (2)), it is possible that it is underestimated. This might lead to an underestimation of the ring current build-up and therefore an underpredicted *Dst*.

[52] In the same style as Figure 13, Figure 14 shows empirical model *Dst* results with two additional smoothed inputs: 3 h averaged B_z (light blue) and density only (orange) along with the 4 min (red) and 180 min (dark blue). As expected, there are no notable differences between the red and orange lines or the light and dark blue lines. That is due to the fact that the predicted *Dst* only depends on density via the pressure correction term. The small-scale variability in the predicted *Dst* is due to the different time resolution of the inputs.

[53] While the *Dst* index is a direct measure of the disturbance in the geomagnetic field produced by near-Earth currents (in particular, the ring current), it is also a good indication of the total kinetic energy of the particles that contribute to this current [*Dessler and Parker*, 1959; *Sckopke*, 1966]. Therefore, assessing the relationship between the solar wind energy input and the *Dst* index is well suited for this study. Figure 15 presents the minimum *Dst* index, both predicted from the *O'Brien and McPherron* [2000] equations (red line) and simulated from the SWMF (black line) as a function of the energy input (as defined in equation (2)). Red triangles represent the predicted value of *Dst* using solar wind input for which only one variable is smoothed (i.e., B_z and density, as described above), while the black diamonds show the complementary simulated results. We note that the empirically predicted *Dst* index shows a linear dependence on the energy input into the magnetosphere, while the simulated *Dst* index appears to be nonlinearly correlated with the energy input.

[54] To illustrate this linearity and nonlinearity, Figure 16 is a repeat of Figure 15 but with the x axis extending to zero.

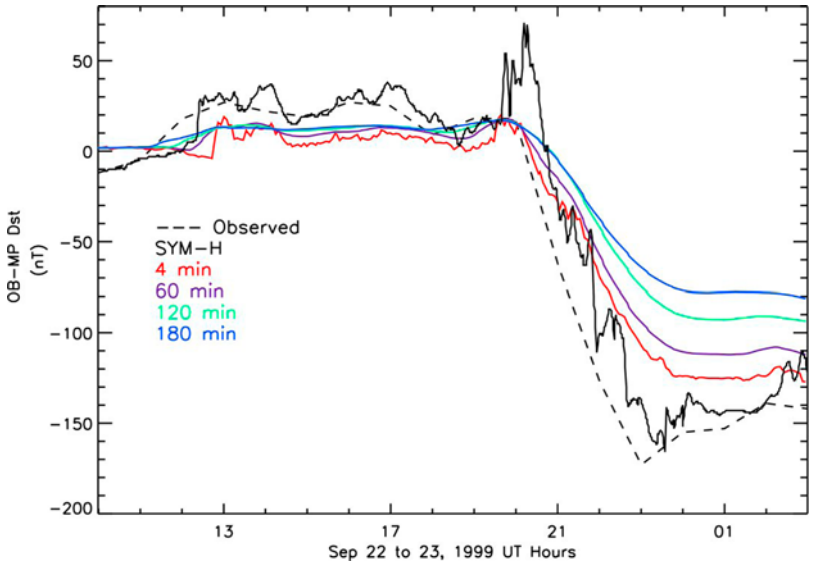

Figure 13. Empirical predictions of *Dst* index results for all averaged inputs for the 22 September 1999 magnetic storm. Each colored line corresponds to different time resolution input data: 4 min (red line), 60 min (purple line), 120 min (green line), 180 min (blue line). The black dashed line represents the observed *Dst* while the black continuous line shows the observed SYM-H index.

The two dashed lines connect the smallest *Dst* value with the origin of the plot. Figure 16 shows that zero energy input produces no disturbance of the geomagnetic field for the case of empirically modeled *Dst*, while a possibly saturation limit is seen at about 100 kV s/m in the profile of the SWMF simulated *Dst* index for this event. Moreover, a minimum threshold of energy input appears to be needed in order to get a magnetospheric response.

[55] One possibility is that the outer magnetosphere is acting as a low-pass filter on the oscillations in the upstream solar wind conditions. As discussed in the introduction, magnetic merging on the dayside does not instantly influence convection within the near-Earth tail, but rather there is a significant time delay as the field lines are convected tailward and reconnect on the nightside. In a forthcoming study by A. J. Ridley (manuscript in preparation, 2010), the SWMF shows a clear decoupling between IMF fluctuations and geospace responses (such as *Dst* and CPCP) for oscillations of less than 30 min. This is fairly consistent with the findings of this real-event study, which show that the in-

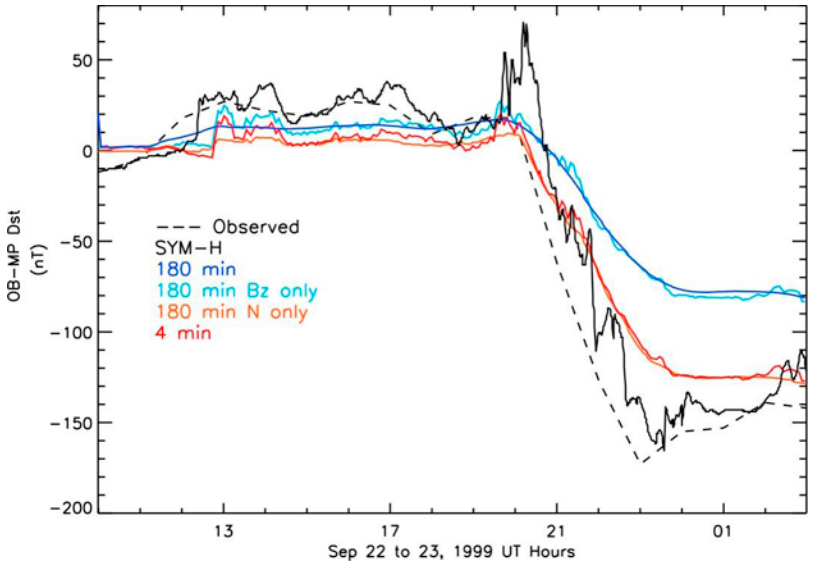

Figure 14. Empirical predictions of the *Dst* index results for averaged inputs for the 22 September 1999 magnetic storm. Each colored line corresponds to different time resolution input data: 4 min (red line), 180 min (dark blue line), 180 min smoothed B_z only (light blue line), 180 min smoothed density only (orange line). The black dashed line represents the observed *Dst* while the black continuous line shows the observed SYM-H index.

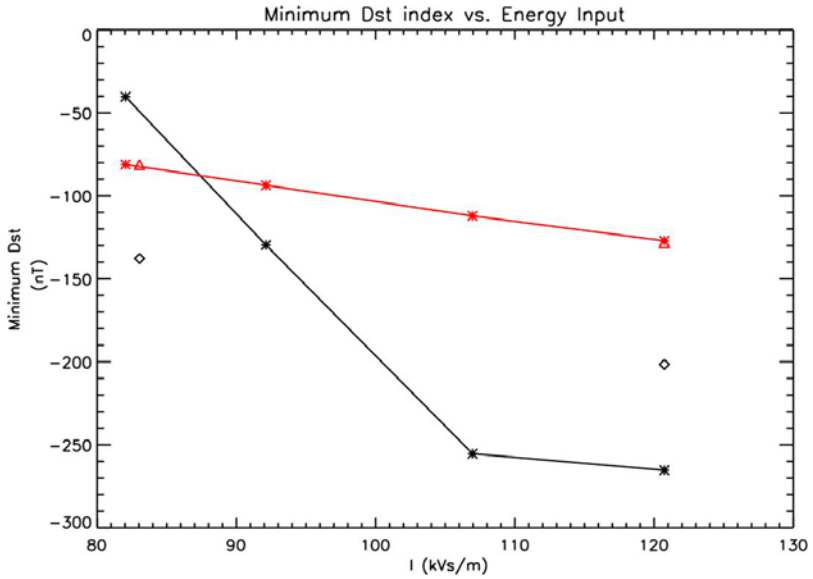

Figure 15. Minimum *Dst* versus energy input. The red line shows the empirical *Dst* prediction results while the black line shows simulation results using SWMF. The red triangles (black diamonds) show the 3 h smoothing of B_z and density using the empirical *Dst* prediction model (MHD simulation).

put power from oscillations of less than 1 h do not significantly change the resulting *Dst* time series.

8. Summary and Conclusions

[56] The 22 September 1999 ICME-driven magnetic storm was simulated using the Space Weather Modeling Framework. ACE satellite measurements were used as the upstream boundary conditions. Analysis of the simulated storm focused on the assessment of the role the transient spikes in the solar wind parameters play in the development of the storm. To accomplish this, we reduced the energy input into the magnetosphere by smoothing all solar wind parameters in the input data with windows of 1, 2, and 3 h. Moreover, just smoothing selective parameters (i.e., IMF B_z and density) allowed us to quantify the role each of them played in the enhancement of the ring current. The results of the simulations were compared with ground-based and satellite-based observations.

[57] Our model produces a two-phase, fast and then slow, recovery phase, in spite of the one-phase recovery of the observed event. The fast recovery occurs when the observed *Dst* is still decreasing, while the slow recovery matches the observed timing and slope. A large cross polar cap potential

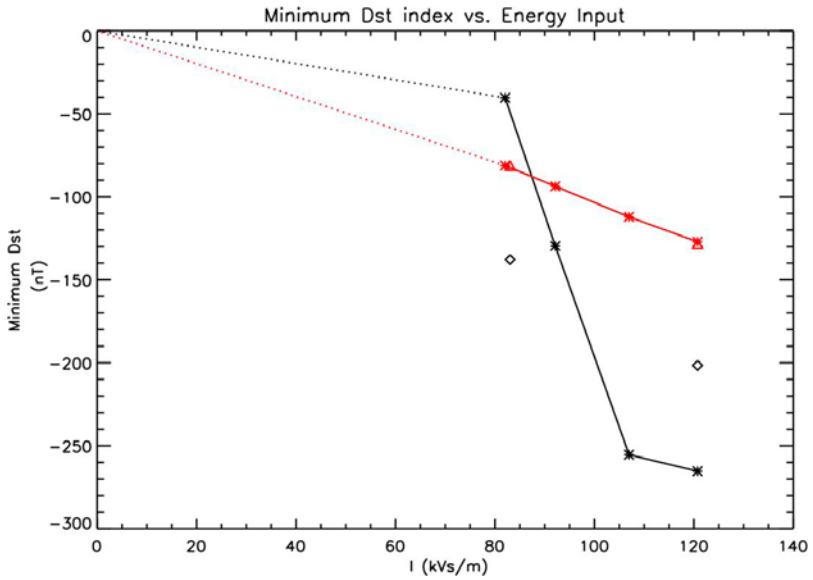

Figure 16. Same as Figure 15 except with a different *x* axis scale (going down to zero).

combined with a low plasma sheet density is most likely responsible for the rapid initial decay of the ring current, similar to the results of *Liemohn et al.* [1999].

[58] Empirical prediction of the *Dst* index not only shows linear relationship with the energy input, but reveals a one-phase recovery *Dst* profile. This is to be expected, since the formulation depends linearly on the solar wind parameters. On the other hand, *Feldstein* [1992] suggested that a nonlinear relationship between the energy input and *Dst* is necessary to better predict the growth and decay of the ring current.

[59] When reducing the energy input more than 13% (that is, smoothing the input with a window larger than 60 min), a weaker ring current forms, therefore a less-intense storm develops. In the same time, the 4 and 60 min time resolution upstream input data produce an overshoot in the estimation of the *Dst* index. This is can be due to the too dense and the too cold plasma sheet the MHD model produces.

[60] Nevertheless, averaging up to 60 min changes the plasma sheet variation as well as the entire magnetosphere and reduces the plasma sheet density and pressure. Small-scale variations of the electric and magnetic fields alter the inner magnetosphere energy density, while rapid small-scale variations produce a more dynamic tail.

[61] Since the plasma sheet is the source region of the ring current particle, changes in its density have a great impact on the ring current intensification. The sudden decay of the plasma sheet particle population along with the weakening of the convection electric field due to changes in the Z component of the interplanetary magnetic field accounts for the slow-recovery phase.

[62] The reconnection rate (modulated by IMF B_z) at the dayside magnetopause controls the ionospheric outflow of particles that will populate the inner magnetosphere. Even though our simulation results indicate no significant differences for CPCP in both hemispheres, for all cases studied, the sharp drop in the midnight plasma sheet density seems to be responsible for the shut down of the fast early recovery. Because our simulations do not explicitly include charge exchange processes, we attribute the late slow decay recovery to the fact that the source region of ring current particles is completely depleted.

[63] Comparison with GOES 8 and GOES 10 magnetic field measurements indicates that varying the energy input produces variations in the magnetic field topology and strength, which in turn modifies the particle orbit, inducing new loss processes. The reduced-energy-input runs reveal a magnetic field that is less stretched with a weaker ring current.

[64] Our global simulation results on the basis of this storm in September 1999 indicate that changes in the energy input change the response of the magnetosphere in a nonlinear manner, as opposed to the linear relationship the empirical model predicts. Our results indicate that a threshold in the energy input is necessary for a ring current to develop, while the short-time fluctuations in the solar wind parameters did not have a significant contribution. On the other hand, while the initial increase in the energy input enhances the magnetospheric response, we observe that a saturation limit is reached as the power transferred to the system is increased, and the growth of ring current is stalled. This implies that not only ion drift loss to the dayside magnetopause is the main loss mechanism that removes the ring current particles during the early recovery phase, but also the existence of an internal feedback mechanism as the magnetosphere acts as a low-pass filter on the interplanetary magnetic field, which limits the energy flow in the magnetosphere.

[65] **Acknowledgments.** Funding for this study was provided by Los Alamos National Security subcontract 33673-001-06, National Science Foundation grant ATM-0802705, and NASA grants NNG05GM48G, NNX08AQ15G, and NNX07AL88G. The authors would like to thank National Space Science Data Center for providing the ACE, GOES 8, and GOES 10 data used in this study. We will also like to thank the entire SWMF software development team for the availability of the code.

[66] Zuyin Pu thanks George Khazanov and another reviewer for their assistance in evaluating this paper.

References

Burton, R. K., R. L. McPherron, and C. T. Russell (1975), An empirical relationship between interplanetary conditions and *Dst*, *J. Geophys. Res.*, *80*(31), 4204–4214.

Chen, M. W., M. Schulz, and L. R. Lyons (1993), Energy content of storm-time ring current from phase space mapping simulations, *Geophys. Res. Lett.*, *20*(16), 1727–1730.

Chen, M. W., L. R. Lyons, and M. Schulz (1994), Simulations of phase space distributions of storm time proton ring current, *J. Geophys. Res.*, *99*(A4), 5745–5759.

Denton, M. H., M. F. Thomsen, H. Korth, S. Lynch, J. C. Zhang, and M. W. Liemohn (2005), Bulk plasma properties at geosynchronous orbit, *J. Geophys. Res.*, *110*, A07223, doi:10.1029/2004JA010861.

Dessler, A. J., and E. N. Parker (1959), Hydromagnetic theory of geomagnetic storms, *J. Geophys. Res.*, *64*(12), 2239–2252.

De Zeeuw, D. L., S. Sazykin, R. A. Wolf, T. I. Gombosi, A. J. Ridley, and G. Tóth (2004), Coupling of a global MHD code and an inner magnetospheric model: Initial results, *J. Geophys. Res.*, *109*, A12219, doi:10.1029/2003JA010366.

Dungey, J. W. (1961), Interplanetary magnetic field and the auroral zones, *Phys. Rev. Lett.*, *6*(2), 47–48.

Dungey, J. W. (1963), The loss of Van Allen electrons due to whistlers, *Planet. Space Sci.*, *11*(6), 591–595.

Ebihara, Y., M.-C. Fok, R. A. Wolf, M. F. Thomsen, and T. E. Moore (2005), Nonlinear impact of plasma sheet density on the storm-time ring current, *J. Geophys. Res.*, *110*, A02208, doi:10.1029/2004JA010435.

Feldstein, Y. I. (1992), Modeling the magnetic field of magnetospheric ring current as a function of interplanetary medium parameters, *Space Sci. Rev.*, *59*, 85–165.

Feldstein, Y. I., L. A. Dremukhina, U. Mall, and J. Woch (2000), On the two-phase decay of the *Dst*-variation, *Geophys. Res. Lett.*, *27*(17), 2813–2816.

Ganushkina, N. Y., et al. (2000), Entry of plasma sheet particles into the inner magnetosphere as observed by Polar/CAMMICE, *J. Geophys. Res.*, *105*(A11), 25,205–25,219.

Ganushkina, N. Y., T. I. Pulkkinen, V. F. Bashkirov, D. N. Baker, and X. Li (2001), Formation of intense nose structures, *Geophys. Res. Lett.*, *28*(3), 491–494.

Ganushkina, N. Y., T. I. Pulkkinen, A. Milillo, and M. Liemohn (2006), Evolution of the proton ring current energy distribution during 21–25 April 2001 storm, *J. Geophys. Res.*, *111*, A11S08, doi:10.1029/2006JA011609.

Greenspan, M. E., and D. C. Hamilton (2000), A test of the Dessler-Parker-Sckopke relation during magnetic storms, *J. Geophys. Res.*, *105*(A3), 5419–5430.

Goldstein, J., B. R. Sandel, W. T. Forrester, and P. H. Reiff (2003), IMF-driven plasmasphere erosion of 10 July 2000, *Geophys. Res. Lett.*, *30*(3), 1146, doi:10.1029/2002GL016478.

Gombosi, T. I., G. Tóth, D. L. De Zeeuw, K. C. Hansen, K. Kabin, and K. G. Powell (2002), Semirelativistic magnetohydrodynamics and physics based convergence acceleration, *J. Comput. Phys.*, *177*(1), 176–205.

Harel, M., R. A. Wolf, P. H. Reiff, R. W. Spiro, W. J. Burke, F. J. Rich, and M. Smiddy (1981), Quantitative simulation of a magnetospheric substorm, 1, Model logic and overview, *J. Geophys. Res.*, *86*, 2217–2241.

Jordanova, V. K., L. M. Kistler, M. F. Thomsen, and C. G. Mouikis (2003), Effects of plasma sheet variability on the fast initial ring current decay, *Geophys. Res. Lett.*, *30*(6), 1311, doi:10.1029/2002GL016576.

Jorgensen, A. M., M. G. Henderson, E. C. Roelof, G. D. Reeves, and H. E. Spence (2001), Charge exchange contribution to the decay of the ring current, measured by energetic neutral atoms (ENAs), *J. Geophys. Res.*, *106*(A2), 1931–1937.

Khazanov, G. V., M. W. Liemohn, M.-C. Fok, T. S. Newman, and A. J. Ridley (2004), Stormtime particle energization with high temporal resolution AMIE potentials, *J. Geophys. Res.*, *109*, A05209, doi:10.1029/2003JA010186.

Kozyra, J. U., M.-C. Fok, E. R. Sanchez, D. S. Evans, D. C. Hamilton, and A. F. Nagy (1998a), The role of precipitation losses in producing the rapid early recovery phase of the Great Magnetic Storm of February 1986, *J. Geophys. Res.*, *103*(A4), 6801–6814.

Kozyra, J. U., V. K. Jordanova, J. E. Borovsky, M. F. Thomsen, D. J. Knipp, D. S. Evans, D. J. McComas, and T. E. Cayton (1998b), Effects of a high-density plasma sheet on ring current development during the November 2–6, 1993, magnetic storm, *J. Geophys. Res.*, *103*(A11), 26,285–26,305.

Kozyra, J. U., M. W. Liemohn, C. R. Clauer, A. J. Ridley, M. F. Thomsen, J. E. Borovsky, J. L. Roeder, V. K. Jordanova, and W. D. Gonzalez (2002), Multi-step *Dst* development and ring current composition changes during the 4–6 June 1991 magnetic storm, *J. Geophys. Res.*, *107*(A8), 1224, doi:10.1029/2001JA000023.

Lavraud, B., and V. K. Jordanova (2007), Modeling the effects of cold-dense and hot-tenuous plasma sheet on proton ring current energy and peak location, *Geophys. Res. Lett.*, *34*, L02102, doi:10.1029/2006GL027566.

Lavraud, B., M. F. Thomsen, S. Wing, M. Fujimoto, M. H. Denton, J. E. Borovsky, A. Aasnes, K. Seki, and J. M. Weygand (2006), Observation of two distinct cold, dense ion populations at geosynchronous orbit: Local time asymmetry, solar wind dependence and origin, *Ann. Geophys.*, *24*, 3451–3465.

Liemohn, M. W., and J. U. Kozyra (2003), Lognormal form of the ring current energy content, *J. Atmos. Sol. Terr. Phys.*, *65*(7), 871–886.

Liemohn, M. W., and J. U. Kozyra (2005), Testing the hypothesis that charge exchange can cause a two-phase decay, in *The Inner Magnetosphere: Physics and Modeling*, *Geophys. Monogr. Ser.*, vol. 155, edited by T. I. Pulkkinen, N. Tsyganenko, and R. H. W. Friedel, pp. 211–225, AGU, Washington, D. C.

Liemohn, M. W., J. U. Kozyra, V. K. Jordanova, G. V. Khazanov, M. F. Thomsen, and T. E. Cayton (1999), Analysis of early phase ring current recovery mechanisms during geomagnetic storms, *Geophys. Res. Lett.*, *26*(18), 2845–2848.

Liemohn, M. W., J. U. Kozyra, M. F. Thomsen, J. L. Roeder, G. Lu, J. E. Borovsky, and T. E. Cayton (2001), Dominant role of the asymmetric ring current in producing the stormtime *Dst**, *J. Geophys. Res.*, *106*(A6), 10,883–10,904.

Lu, G., T. E. Holzer, D. Lummerzheim, J. M. Ruohoniemi, P. Stauning, O. Troshichev, P. T. Newell, M. Brittnacher, and G. Parks (2002), Ionospheric response to the interplanetary magnetic field southward turning: Fast onset and slow reconfiguration, *J. Geophys. Res.*, *107*(A8), 1153, doi:10.1029/2001JA000324.

Murr, D. L., and W. J. Hughes (2007), The coherence between the IMF and high-latitude ionospheric flows: The dayside magnetosphere-ionosphere low-pass filter, *J. Atmos. Sol. Terr. Phys.*, *69*(3), 223–233.

O'Brien, T. P., and R. L. McPherron (2000), An empirical phase space analysis of ring current dynamics: Solar wind control of injection and decay, *J. Geophys. Res.*, *105*(A4), 7707–7719.

Ohtani, S., M. Nos, G. Rostoker, H. Singer, A. T. Y. Lui, and M. Nakamura (2001), Storm-substorm relationship: Contribution of the tail current to *Dst*, *J. Geophys. Res.*, *106*(A10), 21,199–21,209.

Palmroth, M., T. I. Pulkkinen, P. Janhunen, and C.-C. Wu (2003), Stormtime energy transfer in global MHD simulation, *J. Geophys. Res.*, *108*(A1), 1048, doi:10.1029/2002JA009446.

Powell, K. G., P. L. Roe, T. J. Linde, T. I. Gombosi, and D. L. De Zeeuw (1999), A solution-adaptive upwind scheme for ideal magnetohydrodynamics, *J. Comput. Phys.*, *154*(2), 284–309.

Ridley, A. J., and C. R. Clauer (1996), Characterization of the dynamic variations of the dayside high-latitude ionospheric convection reversal boundary and relationship to interplanetary magnetic field orientation, *J. Geophys. Res.*, *101*(A5), 10,919–10,938.

Ridley, A. J., and M. W. Liemohn (2002), A model-derived description of the penetration electric field, *J. Geophys. Res.*, *107*(A8), 1151, doi:10.1029/2001JA000051.

Ridley, A. J., G. Lu, C. R. Clauer, and V. O. Papitashvili (1998), A statistical study of the ionospheric convection response to changing interplanetary magnetic field conditions using the assimilative mapping of ionospheric electrodynamics technique, *J. Geophys. Res.*, *103*(A3), 4023–4039.

Ridley, A. J., T. I. Gombosi, and D. L. DeZeeuw (2004), Ionospheric control of the magnetospheric configuration: Conductance, *Ann. Geophys.*, *22*(2), 567–584.

Ruohoniemi, J. M., and R. A. Greenwald (1998), The response of high-latitude convection to a sudden southward IMF turning, *Geophys. Res. Lett.*, *25*(15), 2913–2916.

Sckopke, N. (1966), A general relation between the energy of trapped particles and the disturbance field near the Earth, *J. Geophys. Res.*, *71*(13), 3125–3130.

Siscoe, G. L., R. L. McPherron, and V. K. Jordanova (2005), Diminished contribution of ram pressure to *Dst* during magnetic storms, *J. Geophys. Res.*, *110*, A12227, doi:10.1029/2005JA011120.

Slinker, S. P., J. A. Fedder, J. M. Ruohoniemi, and J. G. Lyon (2001), Global MHD simulation of the magnetosphere for November 24, 1996, *J. Geophys. Res.*, *106*(A1), 361–380.

Sugiura, M., and T. Kamei (1991), Equatorial *Dst* index 1957–1986, *IAGA Bull. 40*, edited by A. Berthelier and M. Menvielle, Int. Serv. for Geomagn. Indices, Saint-Maur-des-Fosses, France.

Takahashi, S., T. Iyemori, and M. Takeda (1990), A simulation of the stormtime ring current, *Planet. Space Sci.*, *38*, 1133–1141.

Takalo, J., K. Mursula, and J. Timonen (2000), Role of the driver in the dynamics of a coupled-map model of the magnetotail: Does the magnetosphere act as a low-pass filter?, *J. Geophys. Res.*, *105*(A12), 27,665–27,672.

Temerin, M., and X. Li (2002), A new model for the prediction of *Dst* on the basis of the solar wind, *J. Geophys. Res.*, *107*(A12), 1472, doi:10.1029/2001JA007532.

Temerin, M., and X. Li (2006), *Dst* model for 1995–2002, *J. Geophys. Res.*, *111*, A04221, doi:10.1029/2005JA011257.

Toth, G., et al. (2005), Space Weather Modeling Framework: A new tool for the space science community, *J. Geophys. Res.*, *110*, A12226, doi:10.1029/2005JA011126.

Toth, G., D. L. De Zeeuw, T. I. Gombosi, and K. G. Powell (2006), Parallel explicit/implicit time stepping scheme on block-adaptive grid, *J. Comput. Phys.*, *217*(2), 722–758.

Toth, G., D. L. De Zeeuw, T. I. Gombosi, W. B. Manchester, A. J. Ridley, I. V. Sokolov, and I. I. Roussev (2007), Sun-to-thermosphere simulation of the 28–30 October 2003 storm with the Space Weather Modeling Framework, *Space Weather*, *5*, S06003, doi:10.1029/2006SW000272.

Tsurutani, B. T., and W. D. Gonzalez (1997), The interplanetary causes of magnetic storms: A review, in *Magnetic Storms*, *Geophys. Monogr. Ser.*, vol. 98, edited by B. T. Tsurutani et al., pp. 77–90, AGU, Washington, D. C.

Tsurutani, B. T., M. Sugiura, T. Iyemori, B. E. Goldstein, W. D. Gonzalez, S. I. Akasofu, and E. J. Smith (1990), The nonlinear response of AE to the IMF BS driver: A spectral break at 5 hours, *Geophys. Res. Lett.*, *17*(3), 279–282.

Young, D. T., H. Balsiger, and J. Geiss (1982), Correlations of magnetospheric ion composition with geomagnetic and solar activity, *J. Geophys. Res.*, *87*(A11), 9077–9096.

Yu, Y., and A. J. Ridley (2009), Response of the magnetosphere-ionosphere system to a sudden southward turning of interplanetary magnetic field, *J. Geophys. Res.*, *114*, A03216, doi:10.1029/2008JA013292.

Wang, C. B., J. K. Chao, and C.-H. Lin (2003), Influence of the solar wind dynamic pressure on the decay and injection of the ring current, *J. Geophys. Res.*, *108*(A9), 1341, doi:10.1029/2003JA009851.

Weimer, D. R. (2004), Correction to Predicting interplanetary magnetic field (IMF) propagation delay times using the minimum variance technique, *J. Geophys. Res.*, *109*, A12104, doi:10.1029/2004JA010691.

Weimer, D. R., D. M. Ober, N. C. Maynard, M. R. Collier, D. J. McComas, N. F. Ness, C. W. Smith, and J. Watermann (2003), Predicting interplanetary magnetic field (IMF) propagation delay times using the minimum variance technique, *J. Geophys. Res.*, *108*(A1), 1026, doi:10.1029/2002JA009405.

Zhang, J., et al. (2007), Understanding storm-time ring current development through data-model comparisons of a moderate storm, *J. Geophys. Res.*, *112*, A04208, doi:10.1029/2006JA011846.

R. Ilie, M. W. Liemohn, and A. Ridley, Department of Atmospheric, Oceanic and Space Sciences, University of Michigan, Ann Arbor, MI 48109-2143, USA. (rilie@umich.edu)